



## Mesoscopic Percolating Resistance Network in a Strained Manganite Thin Film

Keji Lai *et al.*

*Science* **329**, 190 (2010);

DOI: 10.1126/science.1189925

*This copy is for your personal, non-commercial use only.*

If you wish to distribute this article to others, you can order high-quality copies for your colleagues, clients, or customers by [clicking here](#).

Permission to republish or repurpose articles or portions of articles can be obtained by following the guidelines [here](#).

**The following resources related to this article are available online at [www.sciencemag.org](http://www.sciencemag.org) (this information is current as of July 25, 2012 ):**

**Updated information and services**, including high-resolution figures, can be found in the online version of this article at:

<http://www.sciencemag.org/content/329/5988/190.full.html>

**Supporting Online Material** can be found at:

<http://www.sciencemag.org/content/suppl/2010/07/07/329.5988.190.DC1.html>

This article **cites 30 articles**, 5 of which can be accessed free:

<http://www.sciencemag.org/content/329/5988/190.full.html#ref-list-1>

This article appears in the following **subject collections**:

Physics

<http://www.sciencemag.org/cgi/collection/physics>

15. The Oort cloud has been evolving and losing objects over the lifetime of the solar system. Thus, although the Oort cloud extends to  $a > \sim 10^5$  AU, we only included comets with  $a < 50,000$  AU in our analysis in order to avoid the need to account for this loss. We chose 50,000 AU because this is the largest semimajor axis for which survival for 4 billion years is likely (2).
16. As we were preparing this manuscript, we became aware of (29), who independently found that this mechanism can be responsible for the formation of wide binary star systems.
17. An encounter between the Sun and another star has been invoked before (30, 31) to explain the origin of Sedna, which has an unusual orbit with a semimajor axis of 526 AU and a perihelion distance well beyond the orbits of the planets at 76 AU. See (32) for a detailed early study of this type of encounter.
18. In the real system, there are two dynamical mechanisms for stripping comets away from their original parent stars. The first involves close encounters between the stars. This effect is included in our calculations. The second is caused by close encounters between the comets and the planets in orbit around the parent stars. For computational reasons, this effect was not directly included in these calculations. However, because most comets are stripped by the first process in our simulations, the lack of the second is not significant from the dynamical point of view.
19. H. F. Levison, E. W. Thommes, M. J. Duncan, *Astron. J.* **139**, 1297 (2010).
20. P. R. Weissman, in *Completing the Inventory of the Solar System: A Symposium Held in Conjunction with the 106th Annual Meeting of the ASP*, T. Rettig, J. M. Hahn, Eds., vol. 107 of the Astronomical Society of the Pacific Conference Series (Astronomical Society of the Pacific, San Francisco, 1996), pp. 265–288.
21. The uncertainty in this value is over an order of magnitude. Here, we are simply using the classic value from (20).
22. This estimate assumes that the Saturn-Neptune region originally contained  $35 M_{\odot}$  (26) and that the average mass of a comet is  $4 \times 10^{16}$  g (20), which is very uncertain (21). Thus, it considers all possible sources for Oort cloud comets.
23. It is interesting to speculate whether we would expect to see substantial compositional differences between comets due to our results. These stars formed in the same cluster as the Sun, and thus all the comets formed basically from the same cloud of material. Thus, it is not obvious what to expect.
24. R. Malhotra, *Astron. J.* **110**, 420 (1995).
25. E. W. Thommes, M. J. Duncan, H. F. Levison, *Nature* **402**, 635 (1999).
26. K. Tsiganis, R. Gomes, A. Morbidelli, H. F. Levison, *Nature* **435**, 459 (2005).
27. P. J. Francis, *Astrophys. J.* **635**, 1348 (2005).
28. N. A. Kaib, T. Quinn, *Science* **325**, 1234 (2009).
29. M. B. N. Kouwenhoven *et al.*, *Mon. Not. R. Astron. Soc.* **404**, 1835 (2010).
30. A. Morbidelli, H. F. Levison, *Astron. J.* **128**, 2564 (2004).
31. S. J. Kenyon, B. C. Bromley, *Nature* **432**, 598 (2004).
32. C. J. Clarke, J. E. Pringle, *Mon. Not. R. Astron. Soc.* **261**, 190 (1993).
33. We thank A. Morbidelli and L. Dones for useful discussions. This work was supported by NASA's Astrobiology Institute through a grant to the Goddard Center for Astrobiology. H.F.L. is grateful to NASA for funding through its Operational Support Services and Outer Planets Research programs. M.J.D. is grateful for the hospitality and financial support of the Isaac Newton Institute at Cambridge University, where some of this work was performed. M.J.D. acknowledges the continuing financial support of the Natural Sciences and Engineering Research Council, Canada. R.B. thanks Germany's Helmholtz Alliance for financial support.

#### Supporting Online Material

[www.sciencemag.org/cgi/content/full/science.1187535/DC1](http://www.sciencemag.org/cgi/content/full/science.1187535/DC1)  
SOM Text

Figs. S1 to S3

Table S1

References

Movies S1 to S3

26 January 2010; accepted 24 May 2010

Published online 10 June 2010;

10.1126/science.1187535

Include this information when citing this paper.

# Mesoscopic Percolating Resistance Network in a Strained Manganite Thin Film

Keji Lai,<sup>1\*</sup> Masao Nakamura,<sup>2\*</sup> Worasom Kundhikanjana,<sup>1</sup> Masashi Kawasaki,<sup>2,3</sup> Yoshinori Tokura,<sup>2,4</sup> Michael A. Kelly,<sup>1</sup> Zhi-Xun Shen<sup>1†</sup>

Many unusual behaviors in complex oxides are deeply associated with the spontaneous emergence of microscopic phase separation. Depending on the underlying mechanism, the competing phases can form ordered or random patterns at vastly different length scales. By using a microwave impedance microscope, we observed an orientation-ordered percolating network in strained  $\text{Nd}_{1/2}\text{Sr}_{1/2}\text{MnO}_3$  thin films with a large period of 100 nanometers. The filamentary metallic domains align preferentially along certain crystal axes of the substrate, suggesting the anisotropic elastic strain as the key interaction in this system. The local impedance maps provide mesoscopic electrical information of the hysteretic behavior in strained thin film manganites, suggesting close connection between the glassy order and the colossal magnetoresistance effects at low temperatures.

Doped cuprate superconductors and colossal magnetoresistive (CMR) manganites, the two most studied complex oxides, exhibit rich phase diagrams as a result of the simultaneously active charge, spin, orbital, and lattice degrees of freedom (1, 2). Recent work on

these strongly correlated materials has shown that multiple states can coexist near certain phase boundaries, a scenario known as microscopic phase separation (3). The configurations of these spatially inhomogeneous phases reflect the underlying interactions. When the long-range Coulomb interaction prevails, the competing phases usually form nanometer-scale orders because of the electrostatic energy penalty for macroscopic phase separation (3–6). For self-organized patterns at larger length scales, weaker long-range interactions, such as the elastic strain arising from either the cooperative lattice distortions or lattice mismatch between substrates and epitaxial thin films, become the dominant factors (7–9). Lastly, the unavoidable quenched disorders in real materials always introduce short-range potential fluctua-

tions, which usually smear out the orders or even result in micrometer-sized clusters with random shapes (10).

Many physical properties affected by the phase separation, such as the local density of states (4–6, 11, 12), the local magnetization (13–15), and the atomic displacement (16), can be spatially mapped out by established microscopy tools. For CMR manganites with drastic resistance changes at different temperatures ( $T$ ) and magnetic fields ( $H$ ), the local resistivity ( $\rho$ ) has a large span that makes spatially resolved direct current (DC) measurements challenging. Imaging with high-frequency alternating current (AC)-coupled local probes is thus desirable. We carried out a microwave impedance microscopy (MIM) study (17, 18) on manganite thin films. Unlike other GHz microscopes (19), the cantilever probe is well shielded to reduce the stray fields (18). In the microwave electronics, the high-Q resonator (20) susceptible to environmental conditions is eliminated so that the system can be implemented under variable temperatures (2 to 300 K) and high magnetic fields (9 T). Our cryogenic MIM (21) (fig. S1) is therefore a versatile tool to investigate various electronic phase transitions. Only the imaginary part of the tip-sample impedance (21) (fig. S2) is presented here because the local resistivity information is fully captured by the capacitive channel (MIM-C).

We studied  $\text{Nd}_{1/2}\text{Sr}_{1/2}\text{MnO}_3$  (NSMO) thin films grown on (110)  $\text{SrTiO}_3$  (STO) substrates by pulsed-laser deposition. In single-crystal NSMO, both resistivity and magnetization measurements show a paramagnetic (PM) to ferromagnetic (FM) transition at the Curie temperature  $T_C \sim 250$  K and a charge/orbital-order (COO) transition at  $T_{\text{COO}} \sim 160$  K (22). When a magnetic field is turned on at temperatures below  $T_{\text{COO}}$ , a dramatic first-order

<sup>1</sup>Geballe Laboratory for Advanced Materials, Department of Physics and Department of Applied Physics, Stanford University, CA 94305, USA. <sup>2</sup>Cross-Correlated Materials Group (CMRG) and Correlated Electron Research Group (CERG), RIKEN, Advanced Science Institute (ASI), Wako 351-0198, Japan. <sup>3</sup>WPI-Advanced Institute for Materials Research (AIMR), Tohoku University, Sendai 980-8577, Japan. <sup>4</sup>Department of Applied Physics, University of Tokyo, Tokyo 113-8586, Japan.

\*These authors contributed equally to this work.

†To whom correspondence should be addressed. E-mail: [zxshen@stanford.edu](mailto:zxshen@stanford.edu)

phase transition from the antiferromagnetic COO insulating (COO-I) state to the FM metallic (FM-M) state is observed. We emphasize that two types of

CMR, the  $T$ -driven PM-FM CMR and the low- $T$   $H$ -driven CMR, are widely discussed in the literature (23), and we only focus on the latter in

this work. Recent effort in this model system has been devoted to epitaxial films (24, 25). To date, bulklike behaviors are only seen for films grown

**Fig. 1.** (A) Zero-field  $\rho(T)$  curves of two samples, a (30-nm NSMO/STO) and b (60-nm NSMO/STO). The metallic temperature region between the bulk  $T_C$  (blue) and  $T_{COO}$  (green) is present in sample a but missing in sample b. At low  $T$ ,  $\rho_a(T)$  diverges and  $\rho_b(T)$  saturates. (B) The AFM surface topography contains  $\text{MnO}_x$  precipitates ( $\sim 20$  nm in height) and corrugations. Crystal axes of the STO substrate are indicated. (Inset) An atomically flat region 1 to 2  $\mu\text{m}$  in size. Note the different false-color scales between the main image (40 nm) and the inset (2 nm). (C) Cross-sectional TEM image of the NSMO-STO interface of sample a. The good crystallinity and coherent epitaxy are confirmed by a high-resolution TEM picture (inset). (D) Schematics of the system setup (top) and the corresponding lumped-

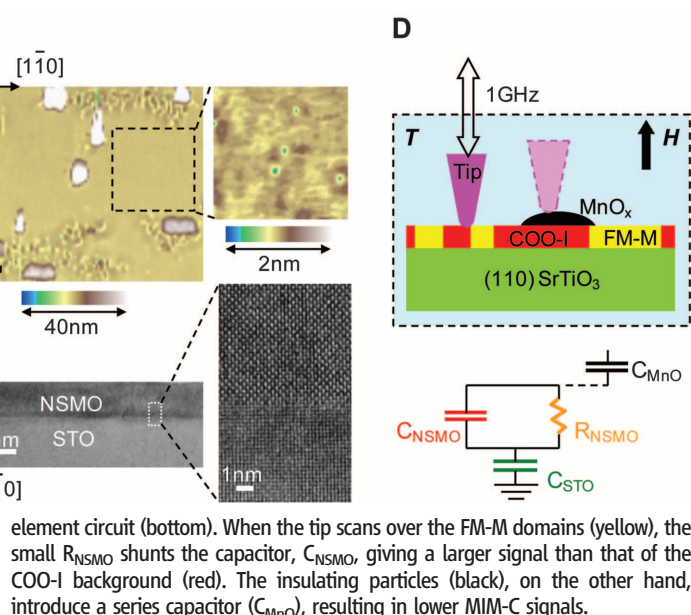
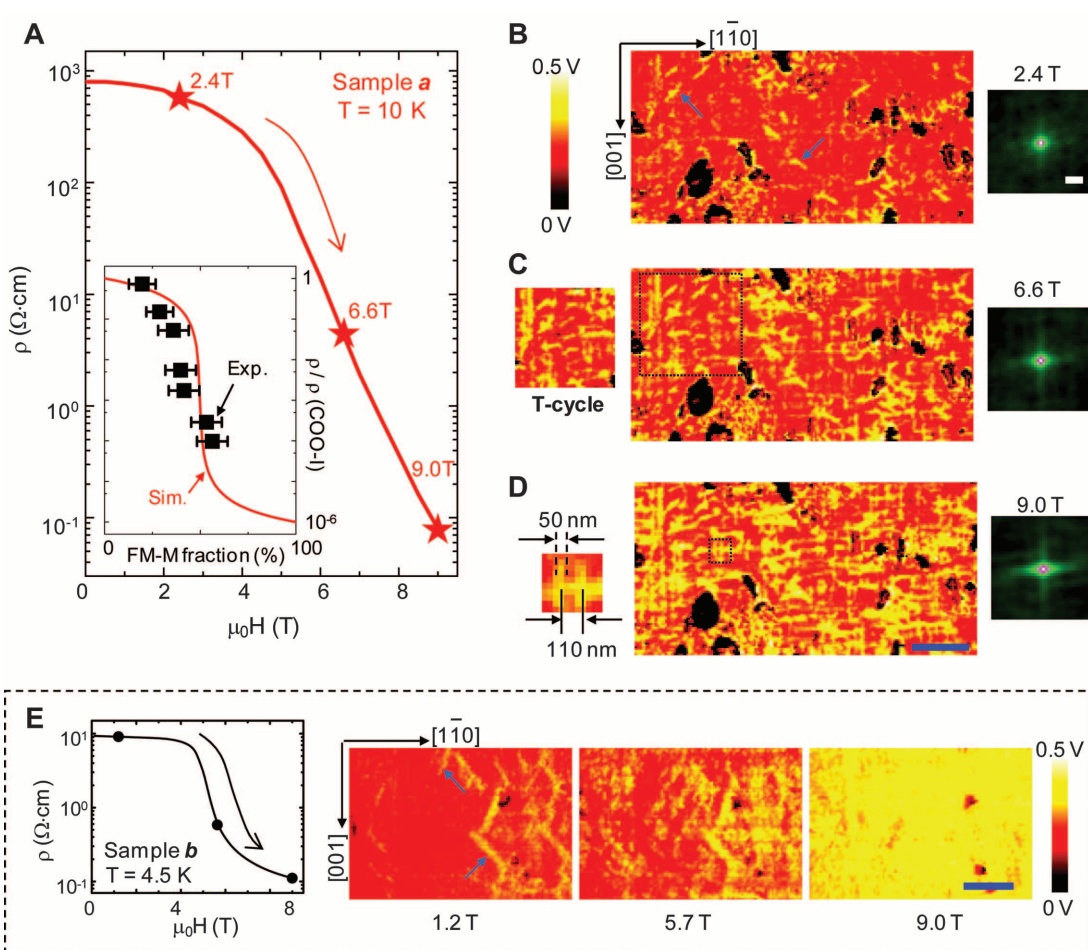


**Fig. 2.** (A)  $\rho_a(H)$  during the field sweep at  $T = 10$  K. The three fields at which MIM images in (B to D) were taken are labeled by the red stars. (Inset) Comparison between the two-dimensional (2D) square-lattice simulation ( $\rho_{\text{COO-I}} \sim 10^3$  ohm-cm and  $\rho_{\text{FM-M}} \sim 10^{-3}$  ohm-cm, see Fig. 3A) and the experimental data. The large error bars and deviations near the percolation transition may result from the surface defects, the finite resolution, and the fact that percolation in NSMO is 3D in nature. For method of estimating the FM-M areal fraction, see fig. S5. (B to D) (Center) Microwave images (6  $\mu\text{m}$  by 3  $\mu\text{m}$ , scale bar = 1  $\mu\text{m}$ ) taken at 10 K and under  $\mu_0 H = 2.4$  T, 6.6 T, and 9.0 T, respectively.  $\text{MnO}_x$  particles appear black in the images. At low fields, some isolated rodlike FM-M domains (yellow) are indicated by blue arrows. [(C) Left inset] Measurement taken at 15 K and 6.5 T after a thermal cycle. [(D) Left inset] Closeup of a small region in (D) (black square) shows the typical width and spacing of the filaments. [(B) to (D) Right images] The center portions of auto-correlation images (scale bar = 0.2  $\mu\text{m}$ ), with a notable center cross seen at 9.0 T. (E) Transport and three MIM images (4.5  $\mu\text{m}$  by 3  $\mu\text{m}$ , scale bar = 1  $\mu\text{m}$ ) of sample b taken at 4.5 K. The low-field FM-M “rods” are indicated by arrows.





on (110) STO substrates, presumably because of the strong dependence on the lattice strain. Even on the same substrate, sample degradation resulting from partial loss of crystallinity and epitaxial coherency (21) (fig. S3) is sometimes detected. We present data from two samples, sample a, in which signatures of  $T_C$  and  $T_{COO}$  are present (Fig. 1A), and for comparison a degraded sample b, which lacks metallic temperature regions. The samples (21) (fig. S4) were characterized by atomic force microscopy (AFM) (Fig. 1B) and cross-sectional transmission electron microscopy (TEM) (Fig. 1C). The surfaces contain micrometer-sized precipitates, most likely  $MnO_x$  (26), and some corrugations next to these particles. In between the defective regions, there exist atomically flat areas where pure electrical signals can be obtained. The contrast in MIM-C images is qualitatively understood by the lumped-element circuit in Fig. 1D.

Simultaneously taken transport data and low- $T$  microwave images (21) (figs. S5 and S6) are shown in Fig. 2, A to D, for sample a and Fig.

2E for sample b. Both the DC voltage ( $<1$  V) and microwave excitation ( $1 \mu W$ ) were kept low to avoid any extrinsic perturbation. The insulating  $MnO_x$  particles behaved as field-independent markers. At low fields where  $\rho$  barely decreases, some rodlike FM-M domains (indicated by blue arrows) tilted with respect to the [001] direction were observed on the COO-I background in both samples. The presence of such low-field conducting domains implies that phase separation already occurs before the magnetic field is turned on. We note that sample b showed larger low-field FM-M areal fraction than sample a. As  $H$  was increased to about 6 to 7 T, metallic areas grew from the low-field nucleation sites; their positions and shapes indicate a certain memory effect (27). In a subsequent experiment, sample a was warmed up to 250 K and cooled back to 15 K at  $H = 0$ . A field of 6.5 T was turned on after this thermal cycle. Most FM-M domains, as shown in Fig. 2C, left inset, reappeared in the same locations compared with the corresponding area in Fig. 2C main (dotted

box), indicative of pinning by an intrinsic long-range energy landscape and short-range disorder potentials. A distinction between the two samples at intermediate fields is that the  $H$ -induced FM-M filaments of sample a (Fig. 2C) show directional ordering and preferentially align along [001] and  $[1\bar{1}0]$  axes of the substrate, whereas no such feature is seen in sample b within our spatial resolution. At about 8 to 9 T, the prominent FM-M filaments in sample a form an interconnected percolating network. Although the smallest measured feature width (30 to 50 nm) may be set by our spatial resolution (21) (fig. S7), the typical spacing  $\sim 100$  nm is resolved here. Because  $\rho_a(H)$  does not show any sign of saturation at 9 T, the FM-M domains should further expand at higher fields.  $\rho_b(H)$ , on the other hand, levels off at 9 T, consistent with the nearly full coverage of FM-M regions.

The salient liquid-crystal-like metallic network accompanying the low- $T$  CMR effect in sample a is not seen by structural characterization and must be electronic in origin. We can obtain some insight by comparing this result with experiments on other manganites. Nanometer-sized domains with no preferred directions were observed in  $La_{1-x}Ca_xMnO_3$  (11, 28) due to Coulomb interaction. Large sub-micrometer clusters were imaged in  $(La,Pr)_{1-x}Ca_xMnO_3$  (16) owing to the strong disorders. In the NSMO films, the elastic strain must play a vital role because neither Coulomb interaction nor quenched disorders can generate such a mesoscopic ordered network (1–3). It is likely that the accommodation strain (7, 14) between the pseudo-cubic FM-M and distorted orthorhombic COO-I phases is responsible for the low-field FM-M rods, which appear in both sample a and b. The more important epitaxial strain imposed by the (110) STO substrate (23, 24), which is crucial for producing the bulklike behaviors, must account for the observed glassy orders in sample a. The lack of a universal form of phase separation in both the PM-FM (11, 28) and the low- $T$  CMR effects (16) (this work) points to the robustness of the phenomenon; the effect occurs because of energetically competing states, whereas the exact CMR magnitude depends on detailed microscopic configurations.

Taking the areal fraction of FM-M states as the probability of connected bonds, we can compare the experimental data to the square-lattice random resistor network simulation (29, 30). Despite some deviations near the threshold (21) (fig. S5), the agreement between experiment and modeling in the Fig. 2A inset shows that the low- $T$  CMR is indeed percolative in nature. Second, the autocorrelation analysis (21) (fig. S8) is performed for Fig. 2, B to D. The nearly circular autocorrelation peak at 2.4 T evolves into a clear center-cross at 9 T with a characteristic length  $\sim 0.5 \mu m$ . In analogy to the stripes or checkerboard patterns seen in cuprates (4–6), the 100-nm period may be set by the long-range

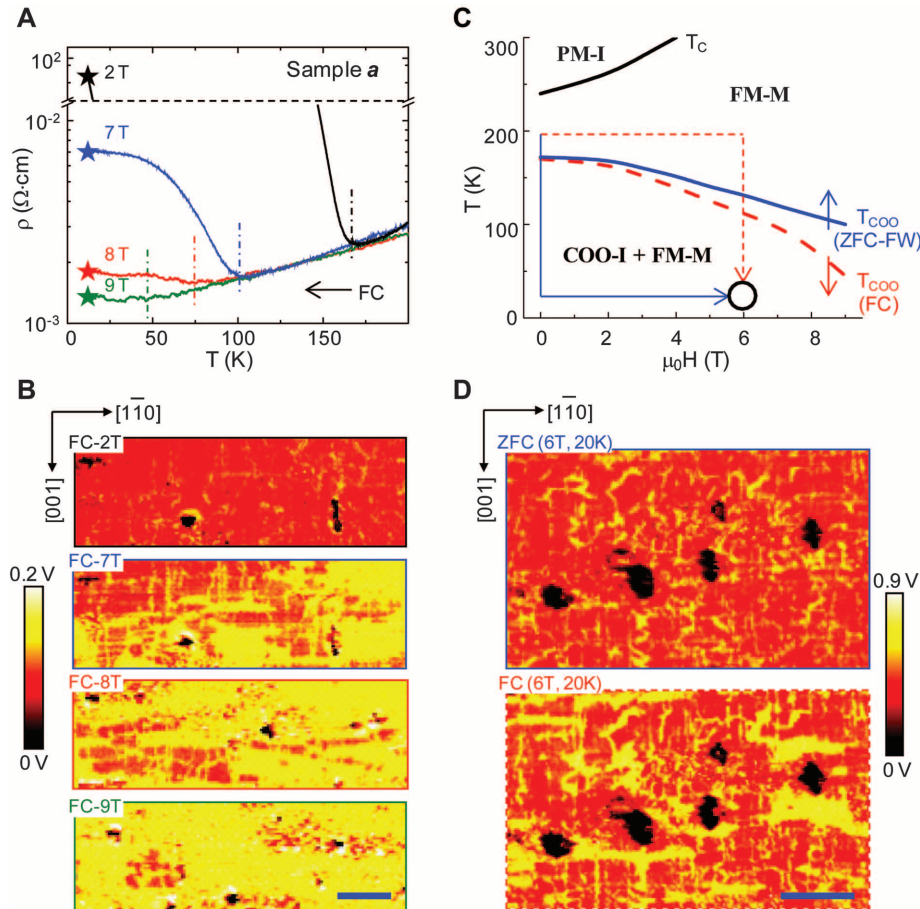


**Fig. 3.** (A) FC resistivity and (B) MIM images ( $6 \mu m$  by  $2 \mu m$ , scale bar =  $1 \mu m$ ) at 2 T, 7 T, 8 T, and 9 T.  $T_{COO}$  values for the four magnitudes of the H-field are denoted in (A) by vertical dash-dot lines, color-coded to match the resistivity curves. (C) Phase diagram of sample a, showing the PM-I, FM-M, and phase coexistence (COO-I + FM-M) regions demarcated by transport signatures  $T_C$  or  $T_{COO}$  from ZFC-FW (field-warm, solid blue line) and FC (dashed red line) processes. Two paths from 200 K and 0 T to 20 K and 6 T are sketched in the plot. (D) MIM images ( $5 \mu m$  by  $3 \mu m$ , scale bar =  $1 \mu m$ ) taken at the same  $T = 20$  K and  $\mu_0 H = 6$  T. The FC image (bottom) contains much bigger conducting domains than the ZFC one (top).

strain field, whereas the typical length of the filaments is determined by the strength of disorders. Interestingly, discernible anisotropy is seen in that the “nematic” domains along the  $[1\bar{1}0]$  direction are statistically more favorable than the  $[001]$  direction, in fair agreement with the transport anisotropy observed in control samples (21) (fig. S9). In the strained NSMO/(110)STO films, the in-plane lattice constant is locked to that of the substrate along the  $[001]$  direction while relaxed along the  $[1\bar{1}0]$  direction (23, 24). At the same time, the charge-ordered planes are parallel to the (100) or (010) planes. Because the low- $T$  CMR effect is accompanied by lattice deformation (22), the metallic domains may tend to expand along the more strain-free axis, resulting in the in-plane anisotropy. The nematic phase at this length scale provides a contrasting framework to understand the “stripe” phenomenon that also breaks in-plane  $C_2$  symmetry at much shorter length scales (31).

The physical picture depicted above is further corroborated by results combining both  $T$  (21) (fig. S10) and  $H$ . In particular, by using a field-cool (FC) process, we can access states with much lower  $\rho$  than the zero-field-cool (ZFC) process discussed so far. Figure 3, A and B, shows the FC curves at four different fields and the corresponding microwave images taken at 12 K, which is below  $T_{\text{COO}}$  for all fields. The continuous COO-I phases at FC-2T break into isolated micrometer-sized domains at FC-7T, which continue to be percolated through by FM-M filaments at FC-8T and shrink down to small droplets at FC-9T. Taking the transport signatures  $T_C$  and  $T_{\text{COO}}$ , we construct the phase diagram of this NSMO/STO sample in Fig. 3C, where phase coexistence is denoted below  $T_{\text{COO}}$ . This phase diagram is reminiscent of the one for single-crystal NSMO (22) except that the reentrant behavior reported there is be-

yond our field range. By using MIM, we can directly study the microscopic origin of the hysteresis. In Fig. 3C, two paths arriving at the same external conditions are shown: the ZFC process from 200 K to 20 K followed by a field sweep to 6 T, or field sweep to 6 T at 200 K before FC to 20 K (21) (fig. S11). The two MIM images in Fig. 3D display remarkably different percolating networks. For the high- $\rho$  (1.4 ohm-cm) ZFC state, glassy FM-M filaments are observed in the COO-I background. For the low- $\rho$  (0.02 ohm-cm) FC state, on the other hand, the FM-M phases occupy a much larger portion and even form micrometer-sized puddles elongated in the  $[1\bar{1}0]$  direction. Although hysteresis during the low- $T$  CMR effect is known in single-crystal NSMO from bulk measurements, tools like MIM enable real-space electrical imaging and demonstrate the strong dependence of phase separation on local disorders and strain fields near the multiphase boundary.

#### References and Notes

1. E. Dagotto, *Science* **309**, 257 (2005).
2. Y. Tokura, *Rep. Prog. Phys.* **69**, 797 (2006).
3. S. Yunoki *et al.*, *Phys. Rev. Lett.* **80**, 845 (1998).
4. M. Vershinin *et al.*, *Science* **303**, 1995 (2004); published online 12 February 2004 (10.1126/science.1093384).
5. T. Hanaguri *et al.*, *Nature* **430**, 1001 (2004).
6. C. Howald, H. Eisaki, N. Kaneko, M. Greven, A. Kapitulnik, *Phys. Rev. B* **67**, 014533 (2003).
7. N. D. Mathur, P. B. Littlewood, *Solid State Commun.* **119**, 271 (2001).
8. K. H. Ahn, T. Lookman, A. R. Bishop, *Nature* **428**, 401 (2004).
9. J. Burgi, A. Moreo, E. Dagotto, *Phys. Rev. Lett.* **92**, 097202 (2004).
10. A. Moreo, M. Mayr, A. Feiguin, S. Yunoki, E. Dagotto, *Phys. Rev. Lett.* **84**, 5568 (2000).
11. M. Fäth *et al.*, *Science* **285**, 1540 (1999).
12. Ch. Renner, G. Aeppli, B.-G. Kim, Y. A. Soh, S. W. Cheong, *Nature* **416**, 518 (2002).
13. L. Zhang, C. Israel, A. Biswas, R. L. Greene, A. de Lozanne, *Science* **298**, 805 (2002); published online 19 September 2002 (10.1126/science.1077346).
14. W. Wu *et al.*, *Nat. Mater.* **5**, 881 (2006).
15. J. C. Loudon, N. D. Mathur, P. A. Midgley, *Nature* **420**, 797 (2002).
16. M. Uehara, S. Mori, C. H. Chen, S.-W. Cheong, *Nature* **399**, 560 (1999).
17. K. Lai, W. Kundhikanjana, M. Kelly, Z. X. Shen, *Rev. Sci. Instrum.* **79**, 063703 (2008).
18. K. Lai, W. Kundhikanjana, M. Kelly, Z. X. Shen, *Phys. Lett.* **93**, 123105 (2008).
19. B. T. Rosner, D. W. van der Weide, *Rev. Sci. Instrum.* **73**, 2505 (2002).
20. Z. Wang *et al.*, *J. Appl. Phys.* **92**, 808 (2002).
21. Materials and methods are available as supporting material on Science Online.
22. H. Kuwahara, Y. Tomioka, A. Asamitsu, Y. Moritomo, Y. Tokura, *Science* **270**, 961 (1995).
23. H. Aliaga *et al.*, *Phys. Rev. B* **68**, 104405 (2003).
24. M. Nakamura, Y. Ogimoto, H. Tamaru, M. Izumi, K. Miyano, *Appl. Phys. Lett.* **86**, 182504 (2005).
25. Y. Wakabayashi *et al.*, *Phys. Rev. Lett.* **96**, 017202 (2006).
26. T. Higuchi *et al.*, *Appl. Phys. Lett.* **95**, 043112 (2009).
27. D. D. Sarma *et al.*, *Phys. Rev. Lett.* **93**, 097202 (2004).
28. J. Tao *et al.*, *Phys. Rev. Lett.* **103**, 097202 (2009).
29. S. Kirkpatrick, *Rev. Mod. Phys.* **45**, 574 (1973).
30. M. Mayr *et al.*, *Phys. Rev. Lett.* **86**, 135 (2001).
31. J. A. Robertson, S. A. Kivelson, E. Fradkin, A. C. Fang, A. Kapitulnik, *Phys. Rev. B* **74**, 134507 (2006).
32. We thank X.-L. Qi, Y. Chen, J. C. Davis, and S. A. Kivelson for valuable discussions. The work is supported by NSF (grants DMR-0906027 and Center of Probing the Nanoscale PHY-0425897), Department of Energy (DE-FG03-01ER45929-A001), Funding Program for World-Leading Innovative R and D on Science and Technology (FIRST) of Japan Society for the Promotion of Science (JSPS), and King Abdullah University of Science and Technology Fellowship (KUS-F1-033-02). Stanford University has filed a patent application with the U.S. Patent Office on the AFM compatible microwave imaging technique. This technology was modified for low-temperature measurement in this report.

#### Supporting Online Material

www.sciencemag.org/cgi/content/full/329/5988/190/DC1  
Materials and Methods  
Figs. S1 to S11

22 March 2010; accepted 3 June 2010  
10.1126/science.1189925

## Predictive Model for Wall-Bounded Turbulent Flow

I. Marusic,\* R. Mathis, N. Hutchins

The behavior of turbulent fluid motion, particularly in the thin chaotic fluid layers immediately adjacent to solid boundaries, can be difficult to understand or predict. These layers account for up to 50% of the aerodynamic drag on modern airliners and occupy the first 100 meters or so of the atmosphere, thus governing wider meteorological phenomena. The physics of these layers is such that the most important processes occur very close to the solid boundary—the region where accurate measurements and simulations are most challenging. We propose a mathematical model to predict the near-wall turbulence given only large-scale information from the outer boundary layer region. This predictive capability may enable new strategies for the control of turbulence and may provide a basis for improved engineering and weather prediction simulations.

Flow over a solid surface or wall produces a region of strong shear due to the no-slip condition at the surface. This strong shear induces tangential stresses at the surface, which,

from an engineering perspective, will lead to energy expenditure (drag for aerodynamic and hydrodynamic vehicles, increased pumping requirements for pipe networks, etc.). Under most

practical conditions, this thin region of shear—known as a boundary layer—is turbulent; the fluid motion is no longer well ordered and instead succumbs to highly chaotic motions, leading to further increases in mechanical losses. Up to half of the fuel burned by a modern airliner during flight is used to overcome drag due to turbulent boundary layers (this proportion is higher still for a large oil tanker or submarine). In addition to energy expenditure, turbulent boundary layers also promote increased mixing, heat transfer, and exchange processes; thus, when they occur on an atmospheric scale, they have important meteorological and climatological implications.

A long-standing challenge has been to understand and predict the behavior of wall-bounded turbulence, especially because the ability to predict

Department of Mechanical Engineering, University of Melbourne, Victoria 3010, Australia.

\*To whom correspondence should be addressed. E-mail: imarusic@unimelb.edu.au